Chemical Engineering Science 327 (2026) 123643

Contents lists available at ScienceDirect

Chemical Engineering Science

journal homepage: www.elsevier.com/locate/ces

Synergistic doping enables efficient nitrate electrosynthesis via dual-regulation of surface polarity and competitive reactions

Xuanni Lin [a], Haixia Zeng [a], Qiannan Liu [a], Dashuai Wang [a,b,*], Qinghua Zhang [a], Jianguo Lu [f], Bin Yang [a], Zhongjian Li [a], Kejun Zhang [c], Evgeniya Sheremet [g], Lecheng Lei [a], Raul D. Rodriguez [g], Yang Hou [a,d,e,*]

[a] Key Laboratory of Biomass Chemical Engineering of Ministry of Education, College of Chemical and Biological Engineering, Zhejiang University, Hangzhou 310027, China
[b] Institute of Zhejiang University - Quzhou, Quzhou 324000, China
[c] Huayou New Energy Technology (Quzhou) Co., Ltd, Quzhou 324000, China
[d] Hydrogen Energy Institute, Zhejiang University, Hangzhou 310027, China
[e] School of Biological and Chemical Engineering, NingboTech University, Ningbo 315100, China
[f] State Key Laboratory of Silicon Materials, School of Materials Science and Engineering, Zhejiang University, Hangzhou 310027, China
[g] Tomsk Polytechnic University, 30 Lenina Ave, Tomsk 634050, Russia

ARTICLE INFO

Keywords:
Electrocatalytic nitrogen oxidation
Nitrate electrosynthesis
Bimetallic doping
Surface polarity
Suppressing oxygen evolution

ABSTRACT

Electrocatalytic nitrogen oxidation (NOR) is an environmentally friendly alternative to conventional energy-demanding industrial nitrate synthesis. However, two major barriers to achieving high NOR efficiency stem from the chemical inertness of N_2 and the competitive nature of the oxygen evolution reaction (OER). Herein, we address the challenges by developing a RuO_2 catalyst synergistically doped with Ni and Co, which effectively boosts N_2 activation while minimizing OER activity. This dual effect is achieved, on the one hand, by Ni-doping, which enhances surface polarity and introduces electron-deficient Ru sites, thereby facilitating interactions with polar intermediates. On the other hand, Co-doping suppresses parasitic oxygen evolution by raising the energy of the OER rate-determining step. Leveraging this synergistic interplay in $Ni_{0.1}Co_{0.2}Ru_{0.7}O_2$-450 yields an outstanding NOR performance, resulting in a high nitrate yield of 726.46 μg h^{-1} mg_{cat}^{-1} and a Faradaic efficiency of 59.65%. These valuable insights will enable the design of efficient bimetal-doped catalysts for nitrate electrosynthesis, resulting in lower energy consumption and a reduced carbon footprint.

1. Introduction

The growing global market for nitrates continues to motivate advances in synthetic production strategies, while the combined Haber-Bosch and Ostwald processes remain the dominant industrial method for nitric acid production (Kong et al., 2022a; Kong et al., 2022b; Li et al., 2022b; Li et al., 2021b; Smith et al., 2020). In this system, ammonia is first synthesized from N_2 and H_2 under harsh conditions (300–500 °C, 100–300 atm), followed by oxidation of the produced NH_3 to nitrogen oxides (400–600 °C, 15–25 MPa) and subsequent absorption in water to form nitrate (Fig. 1a) (Guo et al., 2018; Huang et al., 2023; Smith et al., 2020; van Langevelde et al., 2021; Wang et al., 2021; Wang et al., 2019; Yao et al., 2020). Both steps are highly energy-intensive, demanding substantial electricity, complex infrastructure, and emitting significant greenhouse gases (Wang et al., 2019). Consequently, the development of more efficient and environmentally benign alternatives for nitrate synthesis is urgently needed.

As a sustainable alternative to these energy-intensive processes, the electrocatalytic nitrogen oxidation reaction (NOR) enables direct nitrate synthesis from N_2 under ambient conditions (Fig. 1b) (Li et al., 2025b; Xiang et al., 2024; Yang et al., 2023; Zheng et al., 2024). The NOR process offers a highly controllable and safer alternative that drastically reduces the energy consumption and carbon emissions of conventional nitrate production, while enabling modular, on-demand synthesis that mitigates logistical and safety challenges associated with storage and transport (Chen et al., 2018; Wang et al., 2022b). The NOR process

* Corresponding authors at: Key Laboratory of Biomass Chemical Engineering of Ministry of Education, College of Chemical and Biological Engineering, Zhejiang University, Hangzhou 310027, China.
E-mail addresses: dswang@zju.edu.cn (D. Wang), yhou@zju.edu.cn (Y. Hou).

https://doi.org/10.1016/j.ces.2026.123643
Received 17 November 2025; Received in revised form 3 February 2026; Accepted 17 February 2026
Available online 18 February 2026

involves the adsorption and activation of N_2 molecules on metal active sites to form *NO, and the subsequent non-electrochemical redox reaction of these *NO with O_2 generated via oxygen evolution reaction (OER) to produce nitrate (Kong et al., 2022a; Kuang et al., 2020; Zhang et al., 2021). The transformation of N_2 into the active *NO is widely identified as the rate-determining step (Kuang et al., 2020). Meanwhile, the second step for the formation of nitrate requires moderate OER catalytic activity. Therefore, effective NOR electrocatalysts must balance strong N_2 adsorption/activation with controlled OER activity.

Ruthenium dioxide (RuO_2) is a benchmark electrocatalyst renowned for its exceptional OER activity (Bao et al., 2025; Huang et al., 2025; Wang et al., 2022a). Through structural modification, it was used to elucidate the complementary yet competitive interplay between the OER and NOR. For example, Yan et al. developed a Ru-doped TiO_2/RuO_2 catalyst (Kuang et al., 2020). By incorporating Ru into the TiO_2 lattice, Ru sites with an upshifted d-band center were created to enhance N_2 conversion to NO*, while surface RuO_2 provided controlled OER activity to facilitate nitrate formation without compromising selectivity. Zhang et al. reported that cation vacancies in RuO_2 enhance NOR activity by stabilizing key *OH and facilitating O—O bond cleavage in the rate-determining step of *NN(OH) formation, thereby promoting N_2 activation while modulating OER (Xu et al., 2023). Despite these advances, achieving precise control over both OER suppression and NOR selectivity remains an open challenge.

To address this, we designed a $Ni_xCo_yRu_{(1-x-y)}O_2$-T catalyst to implement a dual-regulation strategy that modulates surface polarity and inhibits the oxygen evolution pathway (x/y: molar ratio of Ni/Co; T: calcination temperature in °C). The optimized $Ni_{0.1}Co_{0.2}Ru_{0.7}O_2$-450 catalyst demonstrated an exceptional NOR activity, yielding a nitrate production rate of 726.46 μg h^{-1} mg_{cat}^{-1} at 1.50 V vs. RHE with a Faradaic efficiency (FE) of 59.65%, and remained stable in operation for over 100 h. Experimental data and density functional theory (DFT) calculations revealed that the doping of Ni enhanced surface polarity and induced more positive charge centers, which enhanced Ru's electro-positivity, facilitating interactions with polar reaction intermediates. Meanwhile, Co doping elevated the reaction energy of the OER rate-determining step, suppressing competitive oxygen evolution. This Ni-Co synergy finely tuned the NOR pathway for superior catalytic performance.

2. Experimental

2.1. Synthesis of $Ni_{0.1}Co_{0.2}Ru_{0.7}O_2$-450

$Ni_{0.1}Co_{0.2}Ru_{0.7}O_2$-450 was synthesized through a multi-step process (Wu et al., 2019). Aqueous solutions of $NiCl_2{\cdot}6H_2O$ (23.77 mg in 10 mL), $CoCl_2{\cdot}6H_2O$ (47.59 mg in 10 mL), and $RuCl_3{\cdot}xH_2O$ (145.18 mg in 10 mL) were individually ultrasonicated for 30 min, mixed, and stirred for 30 min. To the mixture, 5 mL of 1.0 M NaOH was added dropwise under stirring, followed by an additional stirring. The resulting precipitate was hydrothermally treated at 150 °C for 10 h. After filtration and thorough washing with water and ethanol, the product was dried at 60 °C. The dried precursor was finally calcined in flowing air at 450 °C (heating rate: 5 °C·min^{-1}) for 6 h. The synthesis procedures for the other catalysts with varying calcination temperatures and different Ni, Co, and Ru

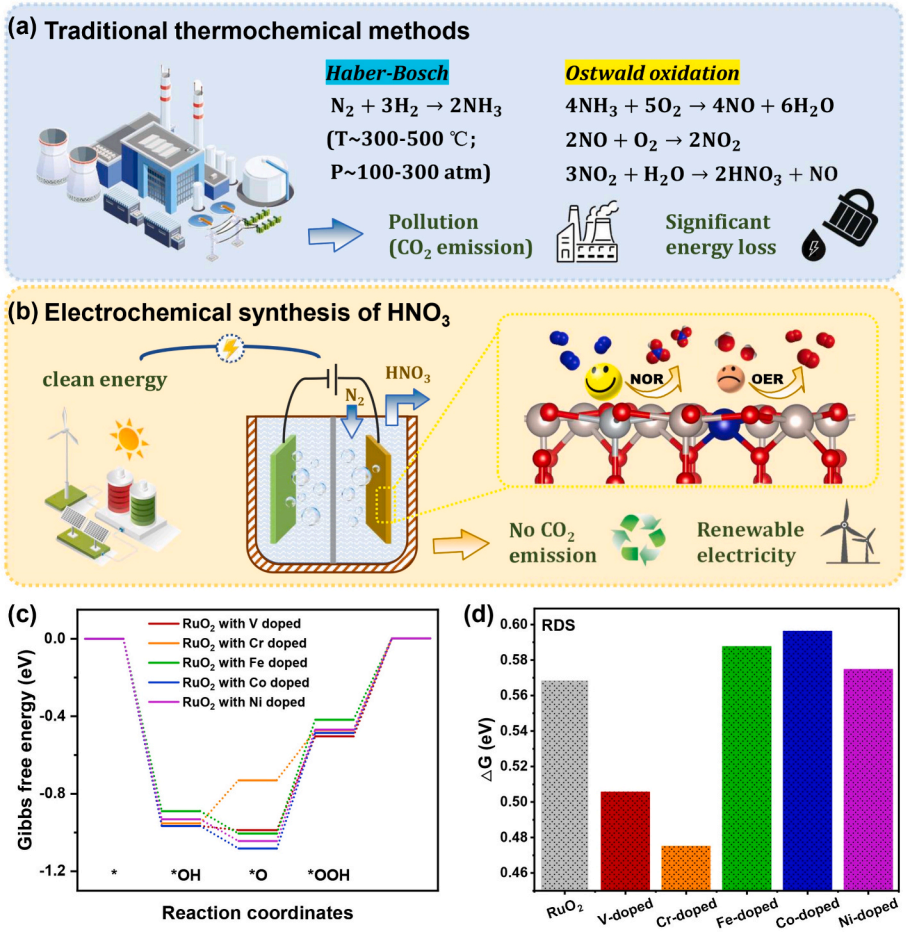

Fig. 1. Optimizing NOR Performance with 3d Metal Dopants. Schematic diagrams of (a) thermochemical and (b) electrochemical methods for nitric acid production. (c) The RDS reaction energies of the OER on the RuO_2 surface with different 3d transition metals dopants. (d) Reaction energy of RDS for OER on RuO_2 and RuO_2 with different 3d transition metals dopants.

compositions ($Ni_xCo_yRu_{(1-x-y)}O_2$-T) were carried out following the same protocol as that of $Ni_{0.1}Co_{0.2}Ru_{0.7}O_2$-450. The specific synthesis conditions are summarized in Table S1.

2.2. Characterizations

The morphologies and compositions of samples were observed with field-emission scanning electron microscope (SEM, SU-8010), transmission electron microscopy (TEM, HT7700) images, and high-resolution TEM (HRTEM, Tecnai G2 F20 S-TWIN) images. Energy dispersive X-ray (EDX) elemental mapping images were obtained on a JEM-2100 electron microscope (HRTEM, 200 kV) equipped with an EDX spectrometer, operating at 120 kV. The crystal structures of samples were characterized by X-ray powder diffraction (XRD, SHIMADZU XRD-6000). The chemical environments of samples were measured with X-ray photoelectron spectroscopy (XPS, Escalab 250Xi). N_2-temperature-programmed desorption (N_2-TPD) measurements were conducted using a Micromeritics 3Flex chemisorption analyzer. N_2 adsorption–desorption isotherms were measured at 77 K (liquid nitrogen temperature) using a Micromeritics ASAP 2460 instrument. Prior to the tests, all samples were degassed under a nitrogen flow at 120 °C for 6 h to remove adsorbed guest molecules and moisture. The specific surface area was calculated by the Brunauer-Emmett-Teller (BET) method.

2.3. Electrochemical measurements

All electrochemical measurements were performed on a CHI 760E electrochemical workstation (Shanghai Chenhua Instrument Co., China) using a three-electrode system with graphite rod, and Hg/HgO electrode as counter and reference electrodes. The working electrode was prepared before electrochemical test. 5 mg of catalyst was dispersed into 1000 μL solution consisting of 950 μL of ethanol, and 50 μL of 5 wt% Nafion solution to achieve a homogeneous ink by ultrasonication for at least 30 min. Next, 50 μL of catalyst ink was pipetted onto carbon paper (1×1 cm^2) with a loading amount of 0.25 mg cm^{-2}. The potentials reported in this work were converted to RHE scale via calibration with the following equation: E (vs. RHE) = E (vs. Hg/HgO) + 0.098 + 0.059 × pH. All experiments were carried out at room temperature (25 °C). For NOR experiments, the electrolyte was purged with N_2 gas for 30 min before measurements. The potentiostatic test was conducted in N_2 saturated 0.1 M KOH solution in a H cell, which was separated by a Nafion membrane. Pure N_2 gas was continuously fed into the anodic compartment during the experiments. All CV or LSV curves were recorded without iR compensation.

2.4. DFT calculations

All calculations of structure relaxation and electronic properties were performed by the Vienna Ab initio Simulation Package with projector-augmented wave pseudopotential (PAW) (Kresse and Furthmüller, 1996a, b). The Perdew-Burke-Ernzerhof (PBE) functional at the generalized gradient approximation (GGA) level was used to treat the exchange–correlation (Hammer et al., 1999; Perdew et al., 1996). A cutoff energy was set to 450 eV, and k-points were sampled using the gamma-centered mesh with a reciprocal space resolution of $2\pi \times 0.05$ $Å^{-1}$ for structural optimization calculations, respectively (Wang et al., 2024; Wang et al., 2023b; Yu et al., 2022a), which ensured that the energy convergence criteria were fulfilled. For the calculation of the DOS, a higher k-point grid density of $2\pi \times 0.04$ $Å^{-1}$ was adopted, which already met the energy convergence accuracy requirements. To avoid any interactions due to the use of periodic boundary conditions, a vacuum separation between two neighboring slabs was set as 15 Å. The solvent effect was described by VASPsol code with the dielectric constant of 80 (Gauthier et al., 2017). For the localized *d*-electrons in Ru, Ni and Co, we employed the DFT + U method, which corrected the self-interaction error and provided a more accurate description of the electronic and magnetic properties of these elements. Specifically, we applied the on-site interaction parameter U_{eff} of 4.88 eV for Ru (Latimer et al., 2017), 6.45 eV for Ni and 3.32 eV for Co (Liu et al., 2015). To describe the electrochemical synthesis of nitrate, the computational hydrogen electrode (CHE) model was used to establish a free energy profile, as proposed by Nørskov and co-workers (Henkelman and Jónsson, 2000; Henkelman et al., 2000; Nørskov et al., 2004).

3. Results and discussions

3.1. Structural design of NOR catalyst via theoretical calculations

Although Ru surfaces can effectively adsorb and activate nitrogen (Han et al., 2021; Kuang et al., 2020; Li et al., 2022a; Nie et al., 2022; Wang et al., 2019), RuO_2's concurrent strong OER activity paradoxically limits its efficacy in the NOR (Kuang et al., 2020; Xu et al., 2023; Yu et al., 2022b). To resolve this, we employed transition metal doping to modulate its OER activity for enhanced NOR performance. DFT calculations were performed to systematically evaluate and compare the reaction energies of the OER rate-determining step (RDS) across a series of dopants, including V, Cr, Fe, Co, and Ni. As shown in Fig. 1c, Co-doped RuO_2 exhibited a higher RDS reaction energy of 0.596 eV compared to other metal dopants, indicating that Co doping effectively moderates the OER activity (Boakye et al., 2024). Further comparison of the OER performance on the RuO_2(1 1 0) surface before and after Co doping (Fig. 1d) revealed that the reaction energy required for the RDS of the OER on RuO_2 is 0.568 eV. On RuO_2 with Co doping, the RDS energy increases to 0.596 eV. This slight increase in energy indicated that Co-doped RuO_2 does not completely suppress OER activity but rather modulates it to a certain extent. In contrast, single-metal doping alone has proven insufficient for simultaneously optimizing nitrogen-containing intermediate transformation and balanced OER activity. We therefore incorporated Ni as a second dopant. Surface electrostatic potential analysis (Fig. S1) revealed that Ni doping enhances surface polarity, creating more positive charge centers and increasing Ru's electro-positivity. This modification promotes the adsorption of polar intermediates, thus facilitating the NOR.

3.2. Synthesis and characterization of NOR catalyst

Scanning electron microscopy (SEM) and transmission electron microscopy (TEM) images (Fig. 2a and b) of $Ni_{0.1}Co_{0.2}Ru_{0.7}O_2$-450 exhibited a well-defined nanoparticle morphology, with an average size of about 4.5 nm. High-resolution TEM (HRTEM) images showed clear lattice fringes corresponding to crystalline RuO_2 domains. The measured interplanar spacings of 2.48 Å, 3.15 Å and 1.68 Å were well indexed to the (1 0 1), (1 1 0) and (2 1 1) planes of RuO_2, respectively (Fig. 2c) (Yan et al., 2022). Control samples, including $Ni_{0.3}Ru_{0.7}O_2$-450, $Co_{0.3}Ru_{0.7}O_2$-450, and RuO_2-450, were synthesized following the same methodology and exhibited morphological features similar to the $Ni_{0.1}Co_{0.2}Ru_{0.7}O_2$-450 (Fig. S2 and Table S1). EDX elemental mapping images demonstrated the homogeneous distribution of Ru, Co, Ni and O elements throughout the whole catalyst (Fig. 2d), revealing the uniform incorporation of Co and Ni into the RuO_2 matrix. Additionally, SEM-EDX analysis revealed that the atomic percentages of Ru, Ni, and Co were 38.7%, 5.7%, and 11.0%, respectively (Fig. 2e), corresponding to a molar ratio of Ru: Ni: Co ≈ 6.84: 1: 1.95. X-ray diffraction (XRD) analysis (Fig. 2f and S3) further corroborated the existence of crystalline RuO_2 phases in $Ni_{0.1}Co_{0.2}Ru_{0.7}O_2$-450, aligning well with the HRTEM imaging observations.

To elucidate the effects of calcination temperature and metal content on the structure of $Ni_xCo_yRu_{(1-x-y)}O_2$-T catalysts, we performed XRD analyses (Figs. S4-S6). When the total doping level $x + y \geq 0.3$, additional diffraction peaks of $NiCo_2O_4$ appeared, suggesting phase segregation at higher Ni and Co contents (Fig. S4c and d). In addition, the continuous shift of the (2 1 1) diffraction peak of RuO_2 to higher angles

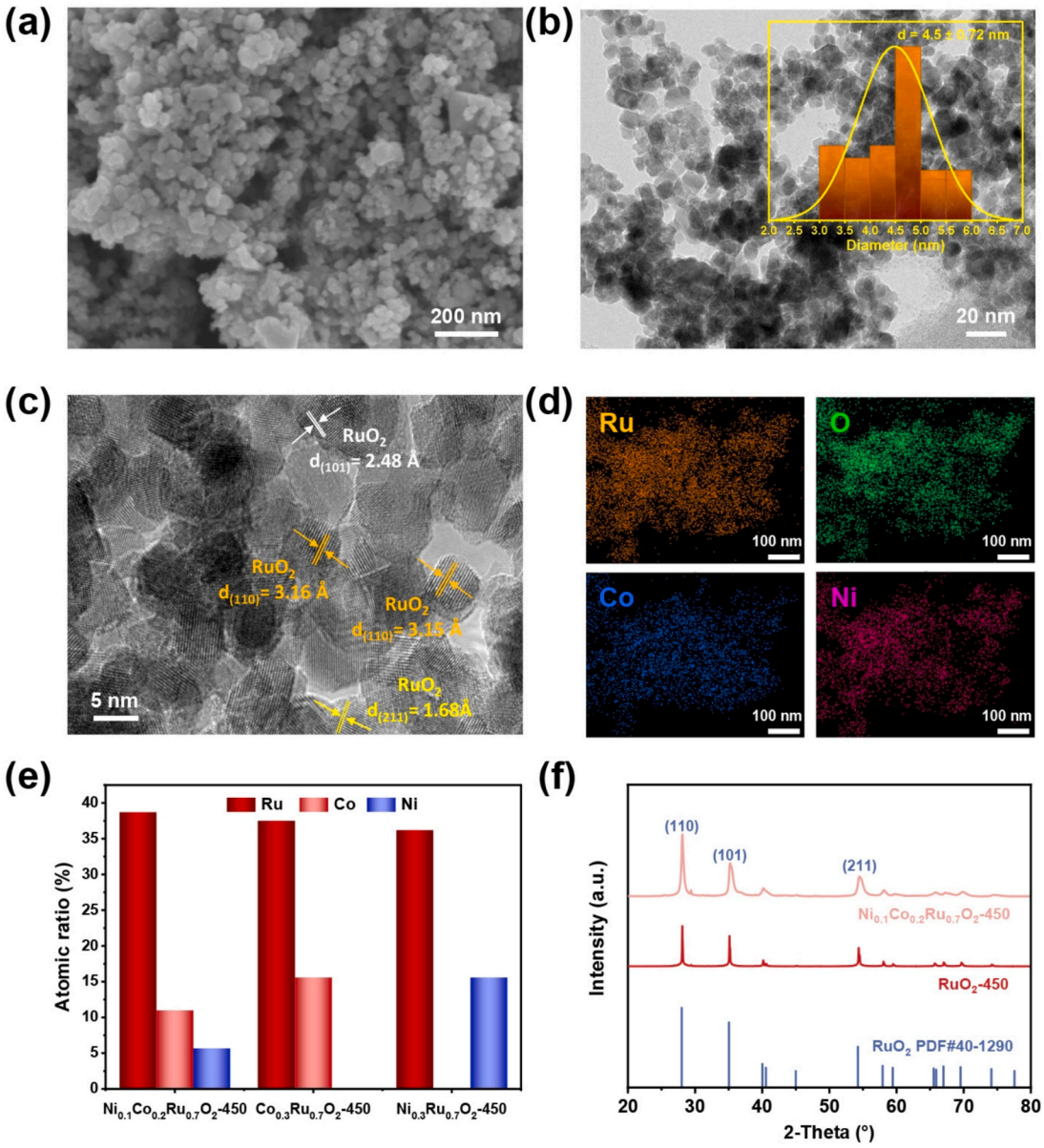

Fig. 2. Morphological and Structural Characterization of NOR Catalyst. (a) SEM, (b) TEM, (c) HRTEM, (d) EDX elemental mapping images of $Ni_{0.1}Co_{0.2}Ru_{0.7}O_2$-450. (e) Elemental atomic ratio of the $Ni_{0.1}Co_{0.2}Ru_{0.7}O_2$-450, $Co_{0.3}Ru_{0.7}O_2$-450, and $Ni_{0.3}Ru_{0.7}O_2$-450. (f) XRD patterns of the $Ni_{0.1}Co_{0.2}Ru_{0.7}O_2$-450 and RuO_2-450.

with increasing Ni and Co doping levels, which can be attributed to the lattice substitution (Fig. S7). We further performed detailed Rietveld refinements on the XRD patterns for representative $Ni_{0.1}Co_{0.2}Ru_{0.7}O_2$-450. The refinements converged successfully with good agreement factors (R_{wp} values $< 7\%$ and R_p values $< 5\%$; Table S2 and Fig. S7), validating the reliability of the structural model. An increase in the lattice parameter b from 22.23 to 22.31 Å was observed upon Ni/Co doping, providing quantitative evidence for Ni/Co dopant incorporation and the associated lattice strain induced by ionic radius mismatch (Gilardi et al., 2017). Notably, $Ni_xCo_yRu_{(1-x-y)}O_2$-450 and $Ni_xCo_yRu_{(1-x-y)}O_2$-600 share similar crystal frameworks, while $NiCo_2O_4$ phase formation occurs more readily at 600 °C (Figs. S4 and S5). The results reveal moderate calcination at 450 °C favors stable Ni and Co incorporation, whereas samples calcined at 300 °C exhibit broader peaks, consistent with reduced crystallinity caused by limited crystal growth (Jain, 2022).

To gain deeper insights into the electronic interactions between Ni, Co, and Ru, we performed X-ray photoelectron spectroscopy (XPS) analysis on $Ni_{0.1}Co_{0.2}Ru_{0.7}O_2$-450, with $Co_{0.3}Ru_{0.7}O_2$-450, $Ni_{0.3}Ru_{0.7}O_2$-450 and RuO_2-450 serving as references. In the Ru 3p spectra (Fig. 3a), a positive shift in the binding energy of Ru 3p was observed for $Ni_{0.1}Co_{0.2}Ru_{0.7}O_2$-450 compared to RuO_2-450. This shift indicated that Ru atoms had lost electrons, leading to a decrease in local electron density. As a result, the oxidation state of Ru in $Ni_{0.1}Co_{0.2}Ru_{0.7}O_2$-450 was higher than + 4. In the Co 2p spectra (Fig. 3b), the peaks at 779.2 eV and 781.2 eV corresponded to Co^{2+} $2p_{3/2}$ and Co^{3+} $2p_{3/2}$, respectively. A negative binding energy shift was observed for $Ni_{0.1}Co_{0.2}Ru_{0.7}O_2$-450 compared to $Co_{0.3}Ru_{0.7}O_2$-450, suggesting a decreased oxidation state of Co. Similarly, the Ni 2p spectra (Fig. 3c) displayed a negative shift in $Ni_{0.1}Co_{0.2}Ru_{0.7}O_2$-450 relative to $Ni_{0.3}Ru_{0.7}O_2$-450, also indicating a lower Ni oxidation state. These findings highlight that the synergistic incorporation of Ni and Co into the RuO_2 reshapes the local electronic structure via charge redistribution.

We further employed N_2-temperature-programmed desorption (N_2-TPD) analysis (Fig. 3d) to investigate the N_2 activation behavior of the catalysts. The desorption temperatures followed the order of $Co_{0.3}Ru_{0.7}O_2$-450 (269 °C) > $Ni_{0.3}Ru_{0.7}O_2$-450 (243 °C) > $Ni_{0.1}Co_{0.2}Ru_{0.7}O_2$-450 (229 °C) > RuO_2-450 (225 °C). First, to exclude the

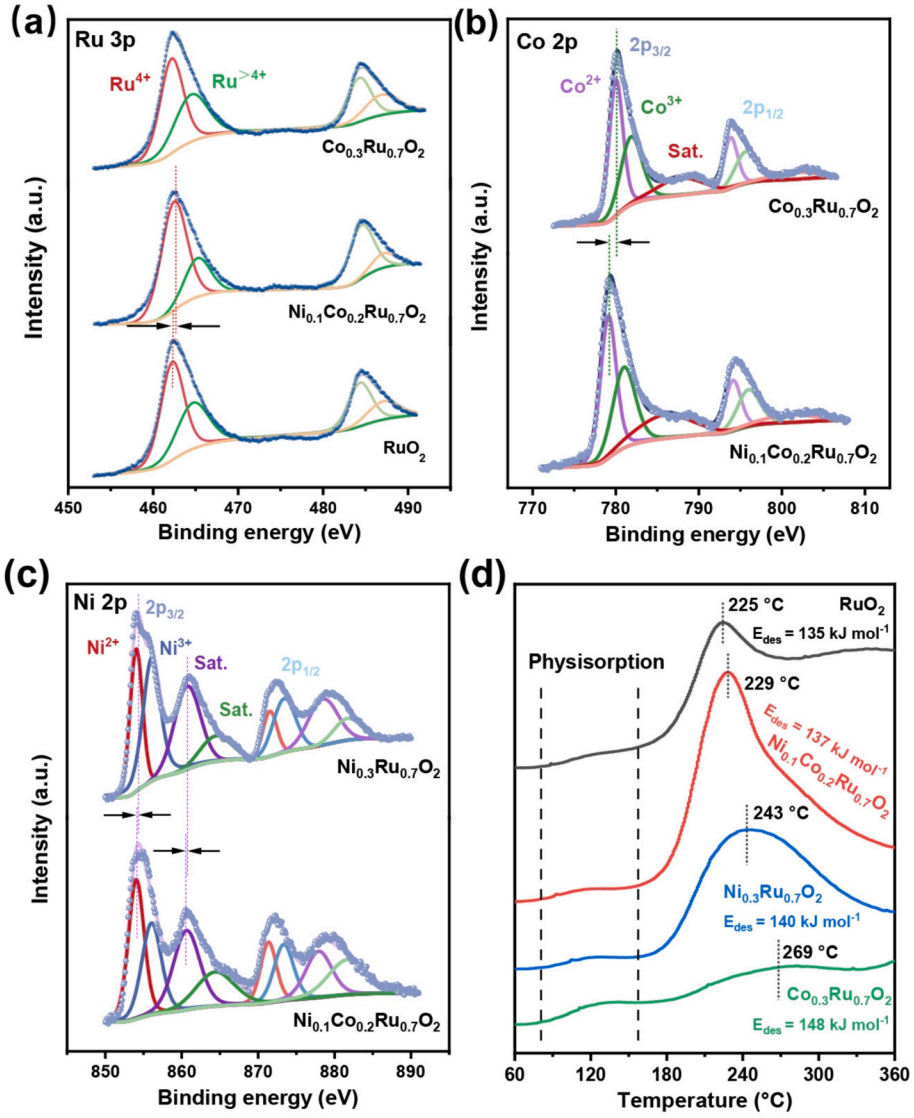

Fig. 3. Electronic Structure and Coordination Environment Characterization of NOR Catalyst. (a-c) XPS spectra of Ru 3p, Co 2p, and Ni 2p regions for $Ni_{0.1}Co_{0.2}Ru_{0.7}O_2$-450, $Co_{0.3}Ru_{0.7}O_2$-450, $Ni_{0.3}Ru_{0.7}O_2$-450 and RuO_2. (d) The N_2-TPD curves of the $Ni_{0.1}Co_{0.2}Ru_{0.7}O_2$-450 and reference samples.

influence of surface area on the N_2-TPD results, N_2 adsorption–desorption isotherms (BET analysis) on $Ni_{0.1}Co_{0.2}Ru_{0.7}O_2$-450, $Ni_{0.3}Ru_{0.7}O_2$-450, $Co_{0.3}Ru_{0.7}O_2$-450 and RuO_2-450 samples were conducted. As shown in Fig. S8, the comparable surface areas of all catalysts suggest that the differences observed in N_2-TPD are likely due to variations in chemical adsorption strength, rather than physical adsorption capacity. Second, in order to quantitatively evaluate the N_2 binding strength, we further performed a Redhead analysis on the N_2-TPD spectra, assuming first-order desorption kinetics. The Redhead analysis yielded desorption activation energies (E_{des}) of 148, 140, 137, and 135 kJ mol^{-1} for $Co_{0.3}Ru_{0.7}O_2$-450, $Ni_{0.3}Ru_{0.7}O_2$-450, $Ni_{0.1}Co_{0.2}Ru_{0.7}O_2$-450, and RuO_2-450, respectively. This trend quantitatively supports our argument that the optimal $Ni_{0.1}Co_{0.2}Ru_{0.7}O_2$-450 possesses an intermediate N_2 binding strength, which is weaker than the singly-doped samples but slightly stronger than pure RuO_2. Third, we also conducted DFT calculations to compare the N_2 adsorption energies on the relevant catalyst surfaces (Fig. S9). The $Ni_{0.1}Co_{0.2}Ru_{0.7}O_2$-450 exhibits a moderate N_2 adsorption energy of −1.371 eV, which is indeed intermediate between the weaker binding on the RuO_2 (−0.935 eV) and the stronger binding on the $Co_{0.3}Ru_{0.7}O_2$-450 (−1.427 eV) and $Ni_{0.3}Ru_{0.7}O_2$-450 (−1.469 eV). Notably, the $Ni_{0.1}Co_{0.2}Ru_{0.7}O_2$-450 demonstrated an enhanced N_2 adsorption capacity compared to RuO_2-450, implying stronger N_2-catalyst interactions and thus facilitating the initial NOR stage. However, too strong binding of the N_2 intermediate to the catalyst surface can block active sites and impair product desorption, ultimately lowering overall efficiency (Li et al., 2022b; Liao et al., 2021; Serrano-Lotina et al., 2017; Yu et al., 2022b). This explains why $Co_{0.3}Ru_{0.7}O_2$-450 and $Ni_{0.3}Ru_{0.7}O_2$-450, despite their stronger N_2 adsorption, perform worse than $Ni_{0.1}Co_{0.2}Ru_{0.7}O_2$-450 in catalytic tests.

3.3. Electrochemical NOR performance

Electrochemical experiments were systematically executed to assess the NOR performance of $Ni_xCo_yRu_{(1-x-y)}O_2$-T catalysts. Ultraviolet–visible (UV–Vis) spectrophotometry was employed to quantify the primary oxidation product nitrate (Fig. S10) (Li et al., 2022a; Wang et al., 2023a). The catalytic performances of the $Ni_xCo_yRu_{(1-x-y)}O_2$-T series (x:y = 1:1, where T represents temperature) obtained through different temperature treatments were evaluated. $Ni_{0.1}Co_{0.1}Ru_{0.8}O_2$-600 exhibited the highest NO_3^- production rate of 527.53 μg h^{-1} mg_{cat}^{-1} and a FE of 50.8% at 1.50 V (Fig. S11). When $x = y < 0.1$, the NOR performance decreased. For $x = y \geq 0.15$, the activity also declined despite higher doping levels, likely due to a segregated $NiCo_2O_4$ phase, which was devoid of catalytic activity (Fig. S4) (Wu et al., 2019). The

$Ni_xCo_yRu_{(1-x-y)}O_2$-450 series (x:y = 1:1) has demonstrated superior NOR performance (Fig. S12). The catalyst with x = y = 0.15 ($Ni_{0.15}Co_{0.15}Ru_{0.7}O_2$-450) achieved the highest NO_3^- production rate of 615.80 μg h^{-1} mg_{cat}^{-1} and a FE of 55.29% at 1.50 V, compared to 592.56 μg h^{-1} mg_{cat}^{-1} and 45.04% for x = y = 0.1 ($Ni_{0.1}Co_{0.1}Ru_{0.8}O_2$-450). Further evaluation of the $Ni_xCo_yRu_{(1-x-y)}O_2$-300 series revealed obviously reduced NOR activity (Fig. S13), which was attributed to deteriorated crystallinity based on XRD analysis (Fig. S6). Combined structural and performance analysis demonstrates that $Ni_xCo_yRu_{(1-x-y)}O_2$-T calcined at 450 °C exhibited the best crystallinity and the highest NOR activity, making this temperature the optimal condition for synthesis.

Given the distinct roles of Ni and Co in the RuO_2 lattice, further research is needed to determine their concentrations and ratios after the optimal temperature is set. The results showed that catalysts doped with either Ni or Co alone exhibited lower performance compared to those co-doped with both elements (Figs. S14 and S15), indicating a synergistic effect. Building on this, our electrochemical and spectroscopic characterization of the catalysts (chronopotentiometry at various potentials, Figs. S16-S21; corresponding UV–Vis absorption spectra, Figs. S22-S27) demonstrated that precise control of the Ni/Co ratio was crucial for maximizing performance. In Fig. 4a and b, $Ni_{0.1}Co_{0.2}Ru_{0.7}O_2$-450 catalyst, with an optimal doping ratio, delivered the highest NOR activity. It achieved a remarkable NO_3^- production rate of 726.46 μg h^{-1} mg_{cat}^{-1} with a FE of 59.65%. Given that the OER is a major competing anodic reaction during NOR, we further performed OER polarization and Tafel analysis for the $Ni_{0.1}Co_{0.2}Ru_{0.7}O_2$-450, $Co_{0.3}Ru_{0.7}O_2$-450, $Ni_{0.3}Ru_{0.7}O_2$-450, and RuO_2-450 (Fig. S28). The results show that the doping of Co and Ni markedly suppresses OER activity concurrently with a rise in Tafel slopes, demonstrating the sluggish OER kinetics of Ni/Co doped samples. The $Ni_{0.1}Co_{0.2}Ru_{0.7}O_2$-450 catalyst, with the highest NOR selectivity, also possesses the most anodically shifted OER polarization curve and the largest Tafel slope. This provides direct evidence that the OER is suppressed in the Ni/Co doped samples, which effectively channels the selectivity toward the NOR pathway. Additionally, $Ni_{0.1}Co_{0.2}Ru_{0.7}O_2$-450 demonstrated exceptional stability and performance advantages, with no significant decay in NO_3^- yield or FE after 100 h of testing at 1.50 V (Fig. 4c). Moreover, the structural integrity of $Ni_{0.1}Co_{0.2}Ru_{0.7}O_2$-450 after the durability test was further confirmed through comprehensive structural characterization. The XRD and TEM images of the post-tested catalyst are essentially identical to those of the pristine sample, with unchanged diffraction peak positions and preserved interplanar spacing (Figs. S29 and S30). The XPS results further show that the chemical states of Ru, Ni, and Co remain unchanged after the durability test (Fig. S31). Consistently, inductively coupled plasma

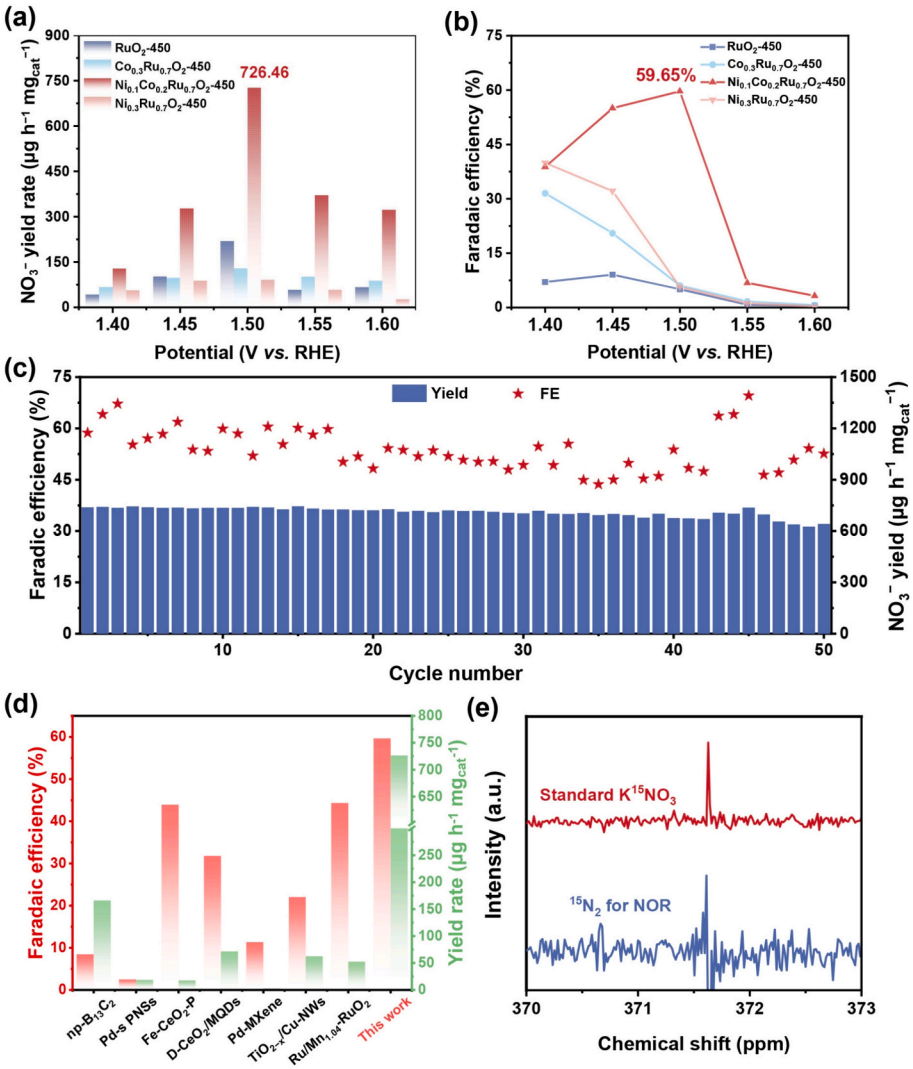

Fig. 4. Electrocatalytic NOR Performance of $Ni_xCo_yRu_{(1-x-y)}O_2$-T. (a) Nitrate yields and (b) FEs of $Ni_{0.1}Co_{0.2}Ru_{0.7}O_2$-450, $Co_{0.3}Ru_{0.7}O_2$-450, $Ni_{0.3}Ru_{0.7}O_2$-450, and RuO_2-450. (c) Nitrate yield rate and FEs of $Ni_{0.1}Co_{0.2}Ru_{0.7}O_2$-450 at 1.50 V during 100-hours tests. (d) Comparison of FE values, nitrate yields, and current density for $Ni_{0.1}Co_{0.2}Ru_{0.7}O_2$-450 with other reported NOR catalysts. (e) ^{15}N NMR spectra for a standard sample of $^{15}NO_3^-$, and the test electrolyte produced from NOR using $^{15}N_2$ feeding gas.

optical emission spectrometry (ICP-OES) measurements of the pre- and post-test catalysts show negligible variation in metal contents (Table S3), further supporting the structural integrity of $Ni_{0.1}Co_{0.2}Ru_{0.7}O_2$-450 throughout the long-term NOR measurement.

The above metrics substantially surpassed those of control catalysts, positioning $Ni_{0.1}Co_{0.2}Ru_{0.7}O_2$-450 among the state-of-the-art NOR catalysts reported in literature (Fig. 4d, Table S4) (Han et al., 2021; Kuang et al., 2020; Li et al., 2025a; Li et al., 2023a; Li et al., 2021a; Mao et al., 2024; Wang et al., 2023a; Zeng et al., 2025). Isotopic validation experiments employing $^{15}N_2$ feedstocks, coupled with ^{15}N nuclear magnetic resonance spectroscopy (NMR) (Fig. 4e and S32), conclusively established N_2 as the nitrate precursor. The absence of any signal in the ^{15}N NMR spectrum of the pristine electrolyte rules out pre-existing ^{15}N-labeled nitrate contamination, while the appearance of a distinct resonance at 371.6 ppm only after reaction under $^{15}N_2$—consistent with the standard $K^{15}NO_3$—thus unambiguously verifying the origin of the nitrogen atom in NO_3^- (Han et al., 2021; Kuang et al., 2020; Wang et al., 2019).

To further investigate the reaction kinetics, the Tafel slopes were determined for the optimal $Ni_{0.1}Co_{0.2}Ru_{0.7}O_2$-450 catalyst, with RuO_2-450, $Ni_{0.3}Ru_{0.7}O_2$-450, and $Co_{0.3}Ru_{0.7}O_2$-450 serving as controls. $Ni_{0.1}Co_{0.2}Ru_{0.7}O_2$-450 exhibited the lowest Tafel slope of 67.95 mV dec^{-1} (Fig. S33), lower than those of RuO_2-450 (96.15 mV dec^{-1}), $Ni_{0.3}Ru_{0.7}O_2$-450 (75.73 mV dec^{-1}), and $Co_{0.3}Ru_{0.7}O_2$-450 (77.20 mV dec^{-1}), indicating a faster NO_3^- formation rate. The electrochemical impedance spectroscopy (EIS) results showed that $Ni_{0.1}Co_{0.2}Ru_{0.7}O_2$-450 had the smallest semicircle among the investigated catalysts, suggesting a lower R_{ct} and more efficient electron transfer (Fig. S34). Furthermore, $Ni_{0.1}Co_{0.2}Ru_{0.7}O_2$-450 possessed the largest electrochemical surface area (ECSA) among the investigated samples (Fig. S35), implying a higher density of accessible active sites and favoring electrolyte interaction during the NOR process.

3.4. Mechanistic insights of NOR

We utilized *in situ* ATR-FTIR spectroscopy to monitor the dynamic evolution of reaction intermediates and compare the surface species on $Ni_{0.1}Co_{0.2}Ru_{0.7}O_2$-450 with those on the control sample, RuO_2-450. Under potentials ranging from 1.35 to 1.65 V, distinct $*NO_3^-$ (1442.5 cm^{-1}), N-N stretching (1126.2 cm^{-1}), and $*NO_2^-$ bending (1292.1 cm^{-1}) peaks were observed on $Ni_{0.1}Co_{0.2}Ru_{0.7}O_2$-450, with increasing intensity at higher potentials (Fig. 5a and S36) (Guo et al., 2023; Li et al., 2022, 2023; Wang et al., 2023). In contrast, analogous signals were also observed on RuO_2-450, confirming that NOR proceeds on both catalysts.

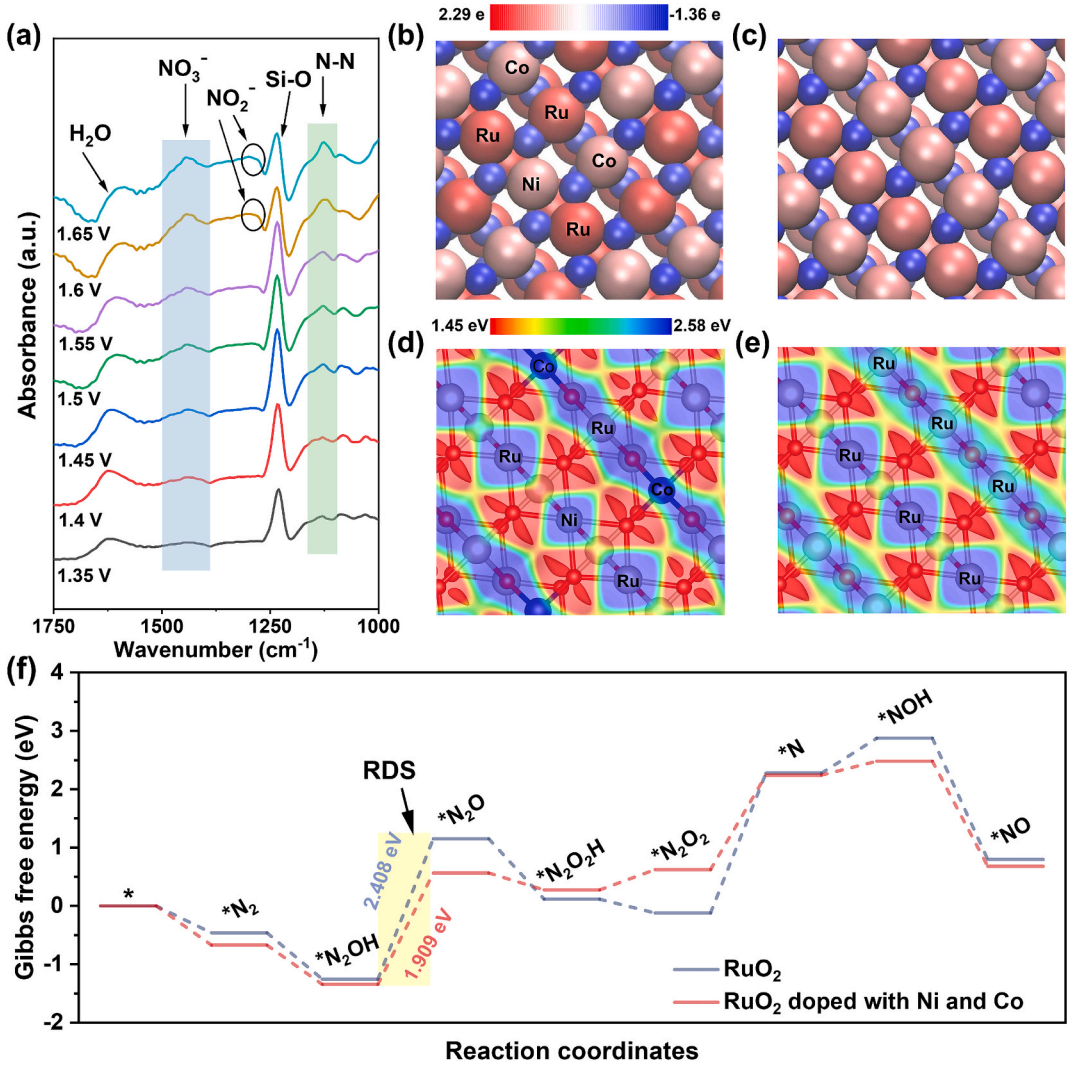

Fig. 5. Mechanistic Insights into NOR. (a) *In situ* ATR-FTIR spectra of $Ni_{0.1}Co_{0.2}Ru_{0.7}O_2$-450 from 1.35 to 1.65 V in N_2-saturated 0.1 M KOH electrolyte. The Bader charge analysis of (b) RuO_2 doped with Ni and Co, and (c) RuO_2, respectively. Charge accumulation and depletion are illustrated by the blue and red regions, respectively. The surface electrostatic potentials of (d) RuO_2 doped with Ni and Co, and (e) RuO_2, respectively. (f) Calculated Gibbs free energy diagrams of NOR on RuO_2 doped with Ni and Co, and RuO_2, respectively.

DFT calculations were systematically performed to elucidate the mechanistic influence of Ni and Co doping on the NOR. Atomic-scale structural models of pristine RuO_2 and RuO_2 doped with Ni and Co were constructed and meticulously optimized (Fig. S37). As revealed by Bader charge analysis, Ru atoms in the Ni and Co doped configuration exhibit an increased tendency toward electron loss (Fig. 5b and c), with an average increase of 1.44 e in electron depletion per Ru site compared to undoped RuO_2. It can be concluded that the valence state of the Ru increased due to the presence of Co and Ni dopants. Combined with the charge density difference analysis (Fig. S38), it was found that charge redistribution occurred on the surface of RuO_2 doped with Ni and Co, leading to a change in surface polarity. This phenomenon is further corroborated by surface electrostatic potential mapping (Fig. 5d and e) (Yang et al., 2024). The consistent results clearly demonstrate an enhanced surface polarity in RuO_2 doped with Ni and Co, which promotes the adsorption and activation of reactants, thereby facilitating NOR.

To further unravel the reaction pathways and the activity of NOR on RuO_2 doped with Ni and Co, as well as on RuO_2 facets, the reaction Gibbs free energy (ΔG) profiles for each intermediate are derived through thermodynamic calculations with implicit solvation effects included using the VASPsol model (Fig. 5f, S39 and S40). The NOR initiates with the adsorption of N_2 on the catalyst surface, followed by its oxidation via the first OH^- ion to form $*N_2OH$. Subsequently, a second OH^- ion captures a hydrogen atom, yielding a H_2O and generating $*N_2O$. It is noteworthy that the formation of $*N_2O$ involves a high reaction energy of 2.408 eV on pristine RuO_2. In contrast, RuO_2 doped with Ni and Co lowers the reaction energy of this critical elementary step, which is identified as the RDS, to 1.909 eV. Furthermore, for the formation of both *N and *NOH, RuO_2 doped with Ni and Co exhibits lower reaction energies than pristine RuO_2. Overall, the NOR reaction was more likely to occur on RuO_2 doped with Ni and Co than on RuO_2, indicating that the Ni and Co doping facilitates the progression of the NOR reaction.

4. Conclusions

We combined Ni and Co doping to synthesize the $Ni_{0.1}Co_{0.2}Ru_{0.7}O_2$-450 that maximizes NOR activity while suppressing oxygen evolution. Our catalyst showed an exceptional nitrate production rate of 726.46 μg h^{-1} mg_{cat}^{-1} and a high FE of 59.65%. Systematic experimental and theoretical analyses showed that Ni doping enhanced surface polarity and introduced electron-deficient Ru sites boosting the adsorption of polar intermediates, while Co doping raised the reaction energy of the RDS step in the oxygen evolution, thereby mitigating competitive OER activity. This Ni and Co synergy rendered the electronic structure of RuO_2 as the optimal for the NOR pathway, resulting in enhanced selectivity and high efficiency for nitrate electrosynthesis. Our work introduces a rational co-doping strategy for designing electrocatalysts for sustainable nitrate electrosynthesis under ambient conditions, bringing us closer to green and scalable nitrogen fixation.

CRediT authorship contribution statement

Xuanni Lin: Writing – original draft, Visualization, Validation, Software, Investigation, Data curation, Conceptualization. **Haixia Zeng:** Writing – original draft, Software, Investigation, Data curation, Conceptualization. **Qiannan Liu:** Supervision, Project administration, Investigation. **Dashuai Wang:** Writing – review & editing, Supervision, Software, Methodology, Formal analysis. **Qinghua Zhang:** Supervision, Project administration. **Jianguo Lu:** Supervision, Project administration. **Bin Yang:** Supervision, Project administration. **Zhongjian Li:** Supervision, Project administration. **Kejun Zhang:** Supervision, Project administration. **Evgeniya Sheremet:** Writing – review & editing, Supervision, Project administration. **Lecheng Lei:** Supervision, Project administration. **Raul D. Rodriguez:** Writing – review & editing, Supervision, Project administration. **Yang Hou:** Writing – review & editing, Supervision, Resources, Funding acquisition, Conceptualization.

Declaration of competing interest

The authors declare that they have no known competing financial interests or personal relationships that could have appeared to influence the work reported in this paper.

Acknowledgements

The authors greatly acknowledge the financial support from the Key Technology Breakthrough Program of Ningbo “Science and Innovation Yongjiang 2035” (2024H024), the development project of Zhejiang Province's “Jianbing” and “Lingyan” (2023C01226), the National Natural Science Foundation of China (U22A20432, 22425805, 22278364, 22211530045, 22208296, 22238008, 22578393), the National Key Research and Development Program of China (2022YFB4002100), the Fundamental Research Funds for the Central Universities (226-2024-00060), the Zhejiang Provincial Natural Science Foundation of China (LD25B060001), the Fundamental Research Funds for the Zhejiang Provincial Universities (226-2025-00224), the China Postdoctoral Science Foundation (2025M780157).

Appendix A. Supplementary data

Supplementary data to this article can be found online at https://doi.org/10.1016/j.ces.2026.123643.

Data availability

The additional characterization data of $Ni_xCo_yRu_{(1-x-y)}O_2$-T are provided in the Supplementary Material. Numerical data for the XRD pattern and *In situ* ATR-FTIR spectra from Figs. 2 and 5, XPS spectra, and N_2-TPD curves from Fig. 3, electrochemical measurements from Fig. 4, and DFT calculations from Fig. 5 that support the findings of this study are available from the corresponding author upon reasonable request.

References

Bao, J., Gu, Y., Su, B., Sun, X., Zhang, H., Wang, K., Lin, X., Yang, C.-J., Yang, B., Li, Z., Dong, C.-L., Zheng, Q., Qiu, M., Lei, L., Yuan, C., Shao, Z., Hou, Y., 2025. Electronic structure-engineered proton depletion interfaces on ternary RuO_2 for ultra-stable kilowatt electrocatalysis. Angew. Chem. Int. Ed., e202515362

Boakye, F.O., Harrath, K., Zhang, D., You, Y., Zhang, W., Wang, Z., Zhang, H., Zhu, J., Long, J., Zhu, J., Yasin, G., Owusu, K.A., Tabish, M., Zhang, L., Wang, D., Shi, X., Jiang, Z., Wu, B., Mai, L., Zhao, W., 2024. Synergistic engineering of dopant and support of Ru oxide catalyst enables ultrahigh performance for acidic oxygen evolution. Adv. Funct. Mater. 34, 2408714.

Chen, J.G., Crooks, R.M., Seefeldt, L.C., Bren, K.L., Bullock, R.M., Darensbourg, M.Y., Holland, P.L., Hoffman, B., Janik, M.J., Jones, A.K., Kanatzidis, M.G., King, P., Lancaster, K.M., Lymar, S.V., Pfromm, P., Schneider, W.F., Schrock, R.R., 2018. Beyond fossil fuel–driven nitrogen transformations. Science 360, eaar6611.

Gauthier, J.A., Dickens, C.F., Chen, L.D., Doyle, A.D., Nørskov, J.K., 2017. Solvation effects for oxygen evolution reaction catalysis on IrO_2(110). J. Phys. Chem. C 121, 11455–11463.

Gilardi, E., Fabbri, E., Bi, L., Rupp, J.L.M., Lippert, T., Pergolesi, D., Traversa, E., 2017. Effect of dopant–host ionic radii mismatch on acceptor-doped barium zirconate microstructure and proton conductivity. J. Phys. Chem. C 121, 9739–9747.

Guo, C., Ran, J., Vasileff, A., Qiao, S.-Z., 2018. Rational design of electrocatalysts and photo(electro)catalysts for nitrogen reduction to ammonia (NH_3) under ambient conditions. Energy Environ. Sci. 11, 45–56.

Guo, H., Guo, Z., Chu, K., Zong, W., Zhu, H., Zhang, L., Liu, C., Liu, T., Hofkens, J., Lai, F., 2023. Polymer-confined pyrolysis promotes the formation of ultrafine single-phase high-entropy alloys: a promising electrocatalyst for oxidation of nitrogen. Adv. Funct. Mater. 33, 2308229.

Hammer, B., Hansen, L.B., Nørskov, J.K., 1999. Improved adsorption energetics within density-functional theory using revised Perdew-Burke-Ernzerhof functionals. Phys. Rev. B 59, 7413–7421.

Han, S., Wang, C., Wang, Y., Yu, Y., Zhang, B., 2021. Electrosynthesis of nitrate via the oxidation of nitrogen on tensile-strained palladium porous nanosheets. Angew. Chem. Int. Ed. 60, 4474–4478.

Henkelman, G., Jónsson, H., 2000. Improved tangent estimate in the nudged elastic band method for finding minimum energy paths and saddle points. J. Chem. Phys. 113, 9978–9985.
Henkelman, G., Uberuaga, B.P., Jónsson, H., 2000. A climbing image nudged elastic band method for finding saddle points and minimum energy paths. J. Chem. Phys. 113, 9901–9904.
Huang, S., Bao, J., Xiang, D., Gao, C., Peng, K., Chen, Q., Ma, S., Jiang, Y., Hu, Z., Zhang, J., 2023. Enhancing electroreduction activity and selectivity of N_2-to-NH_3 through proton-feeding adjustments in Ag@AgP_2@Ni-CoP@C core-shell nanowires. Appl. Catal. b: Environ. Energy 337, 122998.
Huang, S., Jin, T., Zhang, J., Jiang, Y., Hu, J., Niu, H., Naseri, A., Uvdal, K., Hu, Z., Zhang, J., 2025. Sulfur vacancy-engineered Co_9S_8-Ni_3S_4 heterostructure as a hydrogen spillover catalyst for efficient alkaline water splitting. Adv. Sci. e13610.
Jain, R., 2022. A review on the development of XRD in ferrite nanoparticles. J. Supercond. Nov. Magn. 35, 1033–1047.
Kong, Y., Li, Y., Sang, X., Yang, B., Li, Z., Zheng, S., Zhang, Q., Yao, S., Yang, X., Lei, L., Zhou, S., Wu, G., Hou, Y., 2022. Atomically dispersed zinc(I) active sites to accelerate nitrogen reduction kinetics for ammonia electrosynthesis. Adv. Mater. 34, 2103548.
Kong, Y., Wu, L., Yang, X., Li, Y., Zheng, S., Yang, B., Li, Z., Zhang, Q., Zhou, S., Lei, L., Wu, G., Hou, Y., 2022. Accelerating protonation kinetics for ammonia electrosynthesis on single iron sites embedded in carbon with intrinsic defects. Adv. Funct. Mater. 32, 2205409.
Kresse, G., Furthmüller, J., 1996. Efficiency of ab-initio total energy calculations for metals and semiconductors using a plane-wave basis set. Comput. Mater. Sci 6, 15–50.
Kresse, G., Furthmüller, J., 1996. Efficient iterative schemes for ab initio total-energy calculations using a plane-wave basis set. Phys. Rev. B 54, 11169–11186.
Kuang, M., Wang, Y., Fang, W., Tan, H., Chen, M., Yao, J., Liu, C., Xu, J., Zhou, K., Yan, Q., 2020. Efficient nitrate synthesis via ambient nitrogen oxidation with Ru-doped TiO_2/RuO_2 electrocatalysts. Adv. Mater. 32, 2002189.
Latimer, A.A., Abild-Pedersen, F., Nørskov, J.K., 2017. A theoretical study of methanol oxidation on RuO_2(110): bridging the pressure gap. ACS Catal. 7, 4527–4534.
Li, Q., Shen, D., Xiao, Z., Liu, X., Xu, X., Wu, M., Wang, W., Liu, L., Li, Q., Li, X., 2025. Dual-shelled CeO_2 hollow spheres decorated with MXene quantum dots for efficient electrocatalytic nitrogen oxidation. Small 21, 2411665.
Li, Q., Xiao, Z., Jia, W., Li, Q., Li, X., Wang, W., 2023. Copper nanowires decorated with TiO_{2-x} from MXene for enhanced electrocatalytic nitrogen oxidation into nitrate under vacuum assistance. Nano Res. 16, 12357–12362.
Li, T., Han, S., Cheng, C., Wang, Y., Du, X., Yu, Y., Zhang, B., 2022. Sulfate-enabled nitrate synthesis from nitrogen electrooxidation on a rhodium electrocatalyst. Angew. Chem. Int. Ed. 61, e202204541.
Li, T., Han, S., Wang, C., Huang, Y., Wang, Y., Yu, Y., Zhang, B., 2021. Ru-doped Pd nanoparticles for nitrogen electrooxidation to nitrate. ACS Catal. 11, 14032–14037.
Li, T., Han, S., Wang, Y., Zhou, J., Zhang, B., Yu, Y., 2023. A spectroscopic study on nitrogen electrooxidation to nitrate. Angew. Chem. Int. Ed. 62, e202217411.
Li, X., Hai, G., Wan, D.H.C., Liao, Y., Yao, Z., Zhao, F., Huang, L., Zhou, J., Li, G., Chen, G.-F., Wang, F.R., Leung, M.K.H., Wang, H., 2025. Favoring the originally unfavored oxygen for enhancing nitrogen-to-nitrate electroconversion. J. Am. Chem. Soc. 147, 8587–8596.
Li, Y., Ji, Y., Zhao, Y., Chen, J., Zheng, S., Sang, X., Yang, B., Li, Z., Lei, L., Wen, Z., Feng, X., Hou, Y., 2022. Local spin-state tuning of iron single-atom electrocatalyst by S-coordinated doping for kinetics-boosted ammonia synthesis. Adv. Mater. 34, 2202240.
Li, Y., Li, J., Huang, J., Chen, J., Kong, Y., Yang, B., Li, Z., Lei, L., Chai, G., Wen, Z., Dai, L., Hou, Y., 2021. Boosting electroreduction kinetics of nitrogen to ammonia via tuning electron distribution of single-atomic iron sites. Angew. Chem. Int. Ed. 60, 9078–9085.
Liao, W., Qi, L., Wang, Y., Qin, J., Liu, G., Liang, S., He, H., Jiang, L., 2021. Interfacial engineering promoting electrosynthesis of ammonia over Mo/Phosphotungstic acid with high performance. Adv. Funct. Mater. 31, 2009151.
Liu, M., Rong, Z., Malik, R., Canepa, P., Jain, A., Ceder, G., Persson, K.A., 2015. Spinel compounds as multivalent battery cathodes: a systematic evaluation based on ab initio calculations. Energy Environ. Sci. 8, 964–974.
Mao, H., Sun, Y., Li, H., Wu, S., Liu, D., Li, H., Li, S., Ma, T., 2024. Synergy of Pd^{2+}/S^{2-}-doped TiO_2 supported on 2-methylimidazolium-functionalized polypyrrole/graphene oxide for enhanced nitrogen electrooxidation. Adv. Mater. 36, 2313155.
Nørskov, J.K., Rossmeisl, J., Logadottir, A., Lindqvist, L., Kitchin, J.R., Bligaard, T., Jónsson, H., 2004. Origin of the overpotential for oxygen reduction at a fuel-cell cathode. J. Phys. Chem. B 108, 17886–17892.
Nie, Z., Zhang, L., Ding, X., Cong, M., Xu, F., Ma, L., Guo, M., Li, M., Zhang, L., 2022. Catalytic kinetics regulation for enhanced electrochemical nitrogen oxidation by Ru-nanoclusters-coupled Mn_3O_4 catalysts decorated with atomically dispersed Ru atoms. Adv. Mater. 34, 2108180.
Perdew, J.P., Burke, K., Ernzerhof, M., 1996. Generalized gradient approximation made simple. Phys. Rev. Lett. 77, 3865–3868.
Serrano-Lotina, A., Bueno, A.C., Goberna-Selma, C., Avila, P., Bañares, M.A., 2017. NO adsorption and influence of the control of temperature over catalytic test results for NO oxidation. Catal. Today 297, 2–9.
Smith, C., Hill, A.K., Torrente-Murciano, L., 2020. Current and future role of Haber–Bosch ammonia in a carbon-free energy landscape. Energy Environ. Sci. 13, 331–344.
van Langevelde, P.H., Katsounaros, I., Koper, M.T.M., 2021. Electrocatalytic nitrate reduction for sustainable ammonia production. Joule 5, 290–294.
Wang, H., Li, Z., Li, Y., Yang, B., Chen, J., Lei, L., Wang, S., Hou, Y., 2021. An exfoliated iron phosphorus trisulfide nanosheet with rich sulfur vacancy for efficient dinitrogen fixation and Zn-N_2 battery. Nano Energy 81, 105613.
Wang, K., Wang, Y., Yang, B., Li, Z., Qin, X., Zhang, Q., Lei, L., Qiu, M., Wu, G., Hou, Y., 2022. Highly active ruthenium sites stabilized by modulating electron-feeding for sustainable acidic oxygen-evolution electrocatalysis. Energy Environ. Sci. 15, 2356–2365.
Wang, S., Liu, S.S., Cheng, Q.Y., Wang, M.F., Liu, H., Zhang, L.F., Qian, T., Yan, C.L., 2023. "Hole" traps promoting direct nitrate synthesis within flux controlled N_2-rich circumstance. Chem. Eng. J. 455, 140669.
Wang, Y., Lei, X., Zhang, B., Bai, B., Das, P., Azam, T., Xiao, J., Wu, Z.-S., 2024. Breaking the Ru−O−Ru symmetry of a RuO_2 catalyst for sustainable acidic water oxidation. Angew. Chem. Int. Ed. 63, e202316903.
Wang, Y., Li, T., Yu, Y., Zhang, B., 2022. Electrochemical synthesis of nitric acid from nitrogen oxidation. Angew. Chem. Int. Ed. 61, e202115409.
Wang, Y., Yang, R., Ding, Y., Zhang, B., Li, H., Bai, B., Li, M., Cui, Y., Xiao, J., Wu, Z.-S., 2023. Unraveling oxygen vacancy site mechanism of Rh-doped RuO_2 catalyst for long-lasting acidic water oxidation. Nat. Commun. 14, 1412.
Wang, Y., Yu, Y., Jia, R., Zhang, C., Zhang, B., 2019. Electrochemical synthesis of nitric acid from air and ammonia through waste utilization. Natl. Sci. Rev. 6, 730–738.
Wu, Y., Tariq, M., Zaman, W.Q., Sun, W., Zhou, Z., Yang, J., 2019. Ni–Co codoped RuO_2 with outstanding oxygen evolution reaction performance. ACS Appl. Energy Mater. 2, 4105–4110.
Xiang, D., Bao, J., Zhang, L., Xin, P., Yue, C., Naseri, A., Wang, H., Huang, S., Uvdal, K., Hu, Z., 2024. Interfacial electronic structure modulations of Au@CuS with defective Ni-doped CoS_2 facilitates the electroreduction of N_2 into NH_3. Chem. Eng. J. 493, 152456.
Xu, F., Liu, X., Zhang, L., Guo, M., Li, M., Ding, X., Zhang, L., 2023. Revealing and optimizing the dialectical relationship between NOR and OER: cation vacancy engineering enables RuO_2 with unanticipated high electrochemical nitrogen oxidation performance. Adv. Energy Mater. 13, 2300615.
Yan, S., Liao, W.Y., Zhong, M.X., Li, W.M., Wang, C., Pinna, N., Chen, W., Lu, X.F., 2022. Partially oxidized ruthenium aerogel as highly active bifunctional electrocatalyst for overall water splitting in both alkaline and acidic media. Appl. Catal. b: Environ. Energy 307, 121199.
Yang, X., Li, X., Liu, M., Yang, S., Xu, Q., Zeng, G., 2024. Quantitative construction of boronic-ester linkages in covalent organic frameworks for the carbon dioxide reduction. Angew. Chem. Int. Ed. 63, e202317785.
Yang, X., Mukherjee, S., O'Carroll, T., Hou, Y., Singh, M.R., Gauthier, J.A., Wu, G., 2023. Achievements, challenges, and perspectives on nitrogen electrochemistry for carbon-neutral energy technologies. Angew. Chem. Int. Ed. 62, e202215938.
Yao, D., Tang, C., Li, L., Xia, B., Vasileff, A., Jin, H., Zhang, Y., Qiao, S.-Z., 2020. In situ fragmented bismuth nanoparticles for electrocatalytic nitrogen reduction. Adv. Energy Mater. 10, 2001289.
Yu, J., Zeng, Y., Jin, Q., Lin, W., Lu, X., 2022. Hydrogenation of CO_2 to methane over a Ru/$RuTiO_2$ surface: a DFT investigation into the significant role of the RuO_2 overlayer. ACS Catal. 12, 14654–14666.
Yu, M., Fan, G.L., Liu, J.D., Xu, W.C., Li, J.H., Cheng, F.Y., 2022. Self-supported Mo-doped TiO_2 electrode for ambient electrocatalytic nitrogen oxidation. Electrochim. Acta 435, 141333.
Zeng, H., Wang, D., Yang, C.-J., Dong, C.-L., Lin, W., Sang, X., Yang, B., Li, Z., Yao, S., Zhang, Q., Lu, J., Lei, L., Li, Y., Rodriguez, R.D., Hou, Y., 2025. Interfacial electron engineering unlocks efficient nitrate electrosynthesis by balancing nitrogen activation and oxygen evolution. ACS Catal. 15, 9610–9620.
Zhang, Y., Du, F., Wang, R., Ling, X., Wang, X., Shen, Q., Xiong, Y., Li, T., Zhou, Y., Zou, Z., 2021. Electrocatalytic fixation of N_2 into NO_3^-: electron transfer between oxygen vacancies and loaded Au in Nb_2O_{5-x} nanobelts to promote ambient nitrogen oxidation. J. Mater. Chem. A 9, 17442–17450.
Zheng, H., Ma, Z., Liu, Y., Zhang, Y., Ye, J., Debroye, E., Zhang, L., Liu, T., Xie, Y., 2024. Perovskite oxide as a new platform for efficient electrocatalytic nitrogen oxidation. Angew. Chem. Int. Ed. 63, e202316097.